Electrode properties and the dehydrogenation process of amorphous Mg–Ni–La alloys

Lin-Jun Huang [a,*], Yan-Xin Wang [a], Dong-Chang Wu [b], Jian-Guo Tang [a,*], Yao Wang [a], Ji-Xian Liu [a], Zhen Huang [a], Ji-Qing Jiao [a], Jing-Quan Liu [a]

[a] College of Chemistry, Chemical and Environmental Engineering, Qingdao University, Qingdao 266071, China
[b] Department of Materials Physics, Science School, State Key Laboratory of Mechanical Behavior for Materials, Xi'an Jiaotong University, Xi'an 710049, China

HIGHLIGHTS

- $Mg_{65}Ni_{27}La_8$ exhibits a maximum discharge capacity (582 mAh g^{-1}) at room temperature.
- $Mg_{65}Ni_{27}La_8$ releases 4.0 wt.% H during the non-isothermal dehydrogenation process.
- The hydrogen storage capacity of the amorphous phase is larger than that of Mg_2NiH_4.

ABSTRACT

Amorphous Mg–Ni–La hydrogen-storage alloys were prepared by melt-spinning. The phase structures of the ribbons before and after charge/discharge cycling were characterized by X-ray diffraction (XRD) and high resolution transmission electron microscopy (HRTEM) analysis, respectively. The effects of different contents of La are discussed on the basis of discharge-capacity, the morphology, limiting current density and electrochemical impedance spectra of the Mg–Ni–La electrodes. The $Mg_{65}Ni_{27}La_8$ alloy exhibits the best reaction kinetics performance, the lowest contact resistance and a maximum discharge capacity of 582 mAh g^{-1} at room temperature. The non-isothermal dehydrogenation process of $Mg_{65}Ni_{27}La_8$ alloy was analyzed in detail by differential scanning calorimetry (DSC) and thermogravimetry (TG). The experimental results showed a maximum 4.0 wt.% of released hydrogen at a heating rate of 5 °C min^{-1}. The non-isothermal dehydrogenation process of the alloy can be divided in two steps, corresponding to the dehydrogenation of amorphous phase (1.45 wt.% H) and Mg_2NiH_4 (2.55 wt.% H), respectively. It indicated that the amorphous structure was a key factor to achieve high discharge capacity and good cycling stability.

1. Introduction

In the past decade, Mg has been receiving increasing attention for hydrogen storage owing to its high capability of storing hydrogen up to 7.6 wt.% [1–4]. Besides, the abundant resource, environment friendly nature and low costs are also attractive characters of Mg for hydrogen storage applications. However, the practical application of Mg-based alloys is restrained by their poor hydriding–dehydriding kinetics at room temperature and their poor charge–discharge cycle stability [1]. Two major approaches are now considered to solve these problems. One is to reduce the scale of Mg particles [5–8], the other is to add catalytic

elements into Mg to form solid solution or to introduce catalytic additives to form Mg based composites [9–11]. Both are able to improve the hydrogen sorption thermodynamic and kinetic properties of Mg, depending on the scale of the Mg particles, the type and the amount of alloying elements (or additives) that are added [3,4].

A common recognition has been made by many researchers that the decay of discharge capacity for Mg-based hydrogen storage alloys is mainly caused by two reasons, i.e. the corrosion of alloy in alkaline solution and the pulverization of alloy particles during charge–discharge cycles. However, unlike crystalline alloys, amorphous alloys have good resistance for corrosion and pulverization [12–14] because of the absence of any conventional grains and grain boundaries and the continuous volume change when H atoms get in and out the alloy particles. Thus, it is worthwhile to find another reason for the decay of amorphous alloys.

* Corresponding authors. Tel.: +86 532 85951961; fax: +86 532 85951519.
E-mail addresses: newboy66@126.com (L.-J. Huang), tang@qdu.edu.cn (J.-G. Tang).

In our previous work, the crystallization, microstructure and hydrogen storage properties for various melt-spun Mg–Ni–RE (RE is a rare-earth element) and Mg–Cu–RE alloys were studied [15–18]. The amorphous structure was found to be a key factor in achieving a higher discharge capacity. However, little attention has been paid to the dehydrogenation process of amorphous Mg–Ni–RE alloys. Would a structural change in the amorphous alloy take place during this process? An investigation on these would help to understand the hydrogen storage mechanism for amorphous alloys and improve the electrochemical properties.

In present study, melt-spun $Mg_{67.8}Ni_{28.2}La_4$, $Mg_{66.4}Ni_{27.6}La_6$, $Mg_{65}Ni_{27}La_8$ and $Mg_{63.5}Ni_{26.5}La_{10}$ alloys were prepared and a systematic comparison on the effects of different contents of La is carried out. The effects of different contents of La are discussed on the basis of the morphology, limiting current density and electrochemical impedance spectra of the electrodes. The dehydrogenation of $Mg_{65}Ni_{27}La_8$ was investigated by both galvanostatic and non-isothermal methods. The non-isothermal dehydrogenation process of the alloy was studied in detail.

2. Experimental

The Mg–Ni–La alloys ingot were prepared by melting a mixture of pure La metal and Mg–Ni intermediate alloy in a vacuum induction furnace under the protection of argon gas. The purity of the La metal and Mg–Ni intermediate alloy was 99.8 and 99.6 wt.%, respectively. Positive pressure protection and repeated melting were adopted to prevent serious evaporation of Mg and to ensure compositional homogeneity during the preparation of the master alloy ingot. The amorphous ribbons were produced using a single roller melt spinning technique (copper quenching disc with a diameter of 250 mm and surface velocity of about 39 m s^{-1}) in an argon atmosphere of 400 mbar. The as-quenched ribbons were then ball-milled into powder under the protection of an Ar atmosphere with a ball-to-powder weight ratio of 30:1 for 10 min using a specially made mill pot and a SPEX 8000 mill.

The electrochemical measurements were performed using the BT-2000 battery-testing instrument (Arbin). The alloy powder was mixed with nickel powder in a weight ratio of 1:4 (for DSC analysis and electrochemical cycling) and 1:1 (for XRD analysis), and then cold pressed into a piece of nickel foam under a pressure of 20 MPa to prepare the anodes. Ni-oxyhydroxide/dihydroxide was used as cathode and Hg/HgO as reference electrode. The alkaline solution was 6 mol L^{-1} KOH containing 20 g L^{-1} LiOH. For the electrochemical cycling, the anode was charged at 100 mA g^{-1} for 10 h and discharged at 50 mA g^{-1}. The discharge cut-off potential was −0.5 V (vs. Hg/HgO). For DSC and XRD analyses, the anode was first charged–discharged for three cycles for activation, and then charged at 30 mA g^{-1} for 40 h for complete hydrogenation. After charging, the alloy powder (mixed with nickel powder) was separated from the nickel foam.

After the electrodes were completely activated by cycling, the anode polarization, the linear polarization and the electrochemical impedance spectroscopy (EIS) studies were conducted at 50% depth of discharge (DOD) using AMETEK Versa STAT MC electrochemical test system. The anode polarization and the EIS test were carried out at room temperature (27 ± 1 °C). The anode polarization and the linear polarization curves were measured by scanning the electrode potential at a rate of 5 mV s^{-1} from 0 to 600 mV (versus open circuit potential) and 0.1 mV s^{-1} from −5 to 5 mV (versus open circuit potential), respectively. The EIS of the electrodes were obtained in the frequency range of 10 kHz–5 mHz with an AC amplitude of 5 mV under the open circuit condition. The software of the test system was used to analyze the data of EIS.

The non-isothermal dehydrogenation process of the alloy powder was investigated by DSC and TG (NETZSCH-Instruments, STA449C) at a heating rate of 5 °C min^{-1}. In order to exclude the effect of residual water on TG curve of the charged sample, TG curve of an uncharged sample treated in the same condition was used. The corrected TG curve shown in this paper was obtained via multiplying the difference between two curves by five, which could reflect the real relative mass change of $Mg_{65}Ni_{27}La_8$ caused by the dehydrogenation. In order to investigate the non-isothermal dehydrogenation process of $Mg_{65}Ni_{27}La_8$ alloy in detail, the charged $Mg_{65}Ni_{27}La_8$ samples were annealed at 30, 200, 250 and 350 °C using a vacuum anneal furnace. The microstructural characterization of the treated ribbons after charge/discharge cycles was confirmed by high resolution transmission electron microscopy (HRTEM, JEOL-2010). The structure of the treated powder was examined by XRD (Rigaku D, Cu Kα radiation). The crystallinity of the charged sample was calculated using a XRD pattern processing software Jade 5.0 (Materials Data, Inc.). The Ni powder (50 wt.%) in the sample was not taken into account in the calculation.

3. Results and discussions

Fig. 1 presents the X-ray diffraction patterns of the as-quenched $Mg_{67.8}Ni_{28.2}La_4$, $Mg_{66.4}Ni_{27.6}La_6$, $Mg_{65}Ni_{27}La_8$ and $Mg_{63.5}Ni_{26.5}La_{10}$ alloys. The HRTEM images and electron diffraction pattern of different Mg–Ni–La samples show in Fig. 2. It is seen that the as-quenched $Mg_{67.8}Ni_{28.2}La_4$ alloy reveals a nanocrystalline structure with some amorphous phases (see Fig. 2(b)). When the La content exceeds 6 mol%, the alloys $Mg_{66.4}Ni_{27.6}La_6$, $Mg_{65}Ni_{27}La_8$ and $Mg_{63.5}Ni_{26.5}La_{10}$ all show only a broad and diffuse peak (see Fig. 2(a) and (b)), namely the featureless appearance is typical of amorphous structure. It is also seen that the typical amorphous peaks get smoothened and low with the increasing La content, which implies more uniform of elements in the amorphous structure.

Fig. 3 shows the variation of the discharge capacity of the different samples versus the umber of cycles. It can be observed that whatever the cycle number is, $Mg_{65}Ni_{27}La_8$ has the highest capacity and $Mg_{67.8}Ni_{28.2}La_4$ has the lowest one when they are activated. For each composition, with increasing cycle numbers the discharge capacity to reach a maximum after three or four cycles (activation period), and then decreases for upper cycle numbers. The curves of the discharge capacity turn to smooth after 10 cycles. The largest discharge capacity of samples reached 436 mAh g^{-1} for
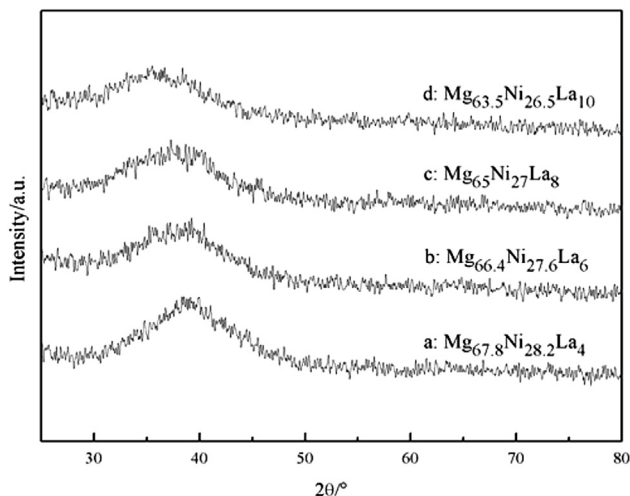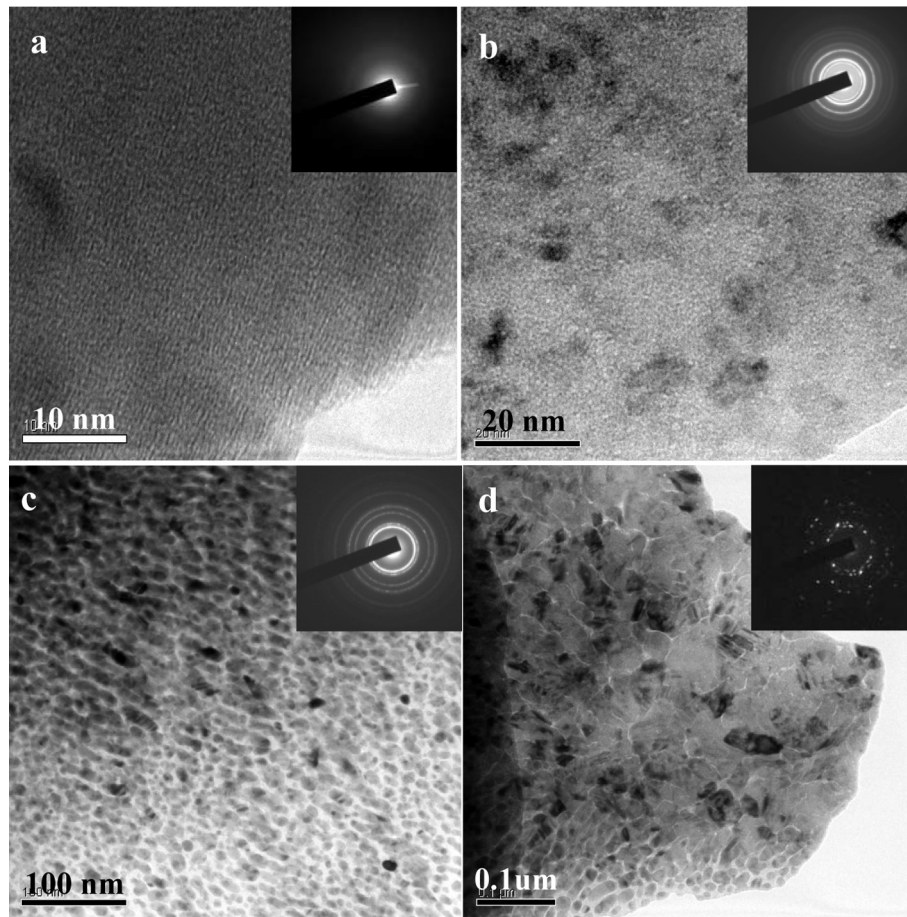

Fig. 1. XRD patterns of the as-quenched Mg–Ni–La alloys.

Fig. 2. HRTEM images and electron diffraction pattern of amorphous sample $Mg_{65}Ni_{27}La_8$ (a), $Mg_{67.8}Ni_{28.2}La_4$ (b), $Mg_{65}Ni_{27}La_8$ alloy charged/discharged for 10 cycles (c) and $Mg_{65}Ni_{27}La_8$ alloy charged/discharged for 20 cycles (d).

4 mol% La, 488 mAh g^{-1} for 6 mol% La, 582 mAh g^{-1} for 8 mol% La and 556 mAh g^{-1} for 10 mol% La.

Table 1 shows the activation period, the maximum capacity and capacity retention at the 20th cycle for different samples. The maximum discharge capacity of $Mg_{65}Ni_{27}La_8$ alloy is comparable

with that of Mg–Ni–Nd alloys [15] and much higher than that of the AB_3 type alloys (about 400 mAh g^{-1}) [19,20]. From above results, it is evident that the increase in discharge capacities is not only a function of the sample composition but also strongly influenced by the amorphous phase proportion in the alloyed material. As the content of La increases, the diffraction peak at about 40° shifts to lower angle (Fig. 1). As we all know, the peak position of diffuse maxima is influenced by the average atomic distances in the amorphous matrix (short-range order). In Fig. 1, the peak shift to lower positions is perhaps related to the larger atomic radius of the additional La and consequently, the higher the concentration the lower the position of the diffuse peak. That would enhance hydrogen diffusivity and solubility in amorphous and disordered structures, associated with the wide energy distribution of the available sites for hydrogen in the glassy structure as well as avoiding the long-range diffusion of hydrogen through an already formed hydride. However, although the amorphous samples can
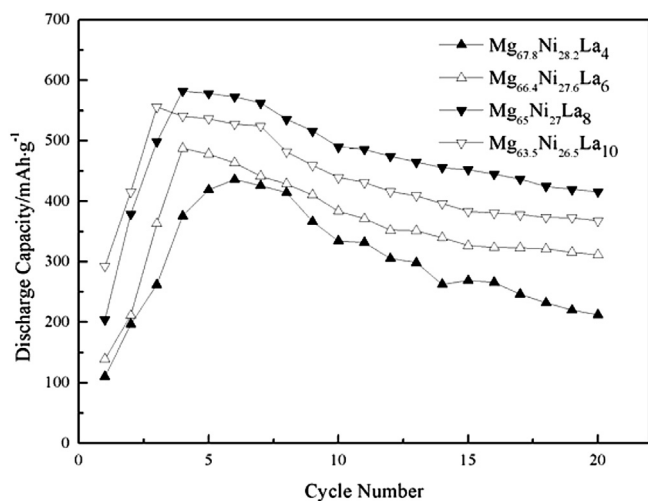

Fig. 3. Variation of the discharge capacity versus the cycle number for the different samples.

Table 1
The activation period, the maximum discharge capacity (C_{max}), the discharge capacity after 20 cycles (C_{20}) and capacity retention for Mg–Ni–La samples.

Samples	Activation period/cycle	C_{max}/mAh g^{-1}	C_{20}/mAh g^{-1}	Capacity retention/%
$Mg_{67.8}Ni_{28.2}La_4$	6	436	212	48.6
$Mg_{66.4}Ni_{27.6}La_6$	4	488	312	63.9
$Mg_{65}Ni_{27}La_8$	4	582	415	71.4
$Mg_{63.5}Ni_{26.5}La_{10}$	3	556	368	66.1
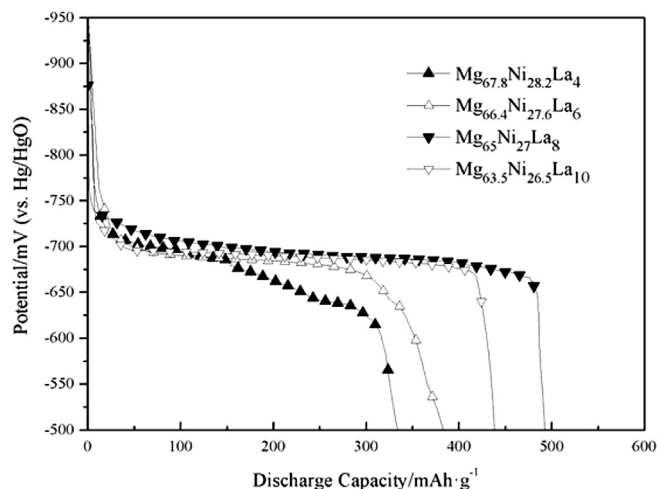
Fig. 4. Relationship of voltage and the discharge capacities for Mg−Ni−La alloys (at the 10 cycles).

Fig. 6. Anode polarization curves of the Mg−Ni−La electrodes at 50% depth of discharge at 27 °C.

achieve quite high discharge capacity, the decay of discharge capacity is still significant (see Table 1). This phenomenon is much more obvious in other amorphous electrodes produced by high-energy milling [21,22].

Fig. 2(c) showed the HRTEM image and electron diffraction pattern of amorphous sample $Mg_{65}Ni_{27}La_8$ charged/discharged for ten cycles. It exhibits that amorphous sample that charged/discharged hydrogen after 10 cycles results in the formation of nanocrystals structures besides a few residual amorphous phases. Charging/discharging after ten cycles causes formation of a coarser grained crystalline phase Mg_2Ni with average grain size in the range 20−30 nm (Fig. 2(c) and Fig. 11). The HRTEM image and electron diffraction pattern of amorphous sample $Mg_{65}Ni_{27}La_8$ charged/discharged for twenty cycles are showed in Fig. 2(d). It is found that after twenty cycles of charging/discharging the amorphous samples are almost completely crystallized with the biggest grain size about 100 nm (Fig. 2(d)) are present, indicating that the amorphous phase formed at beginning is crystallized gradually with the proceeding of hydrogenation/dehydrogenation (Fig. 2(a), (c) and (d)).
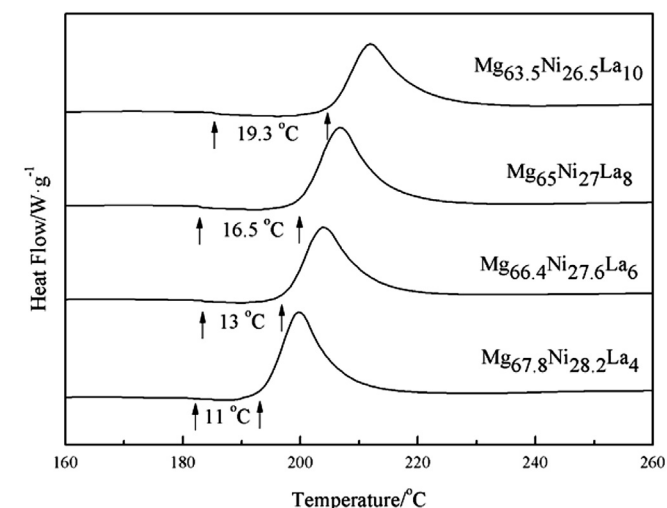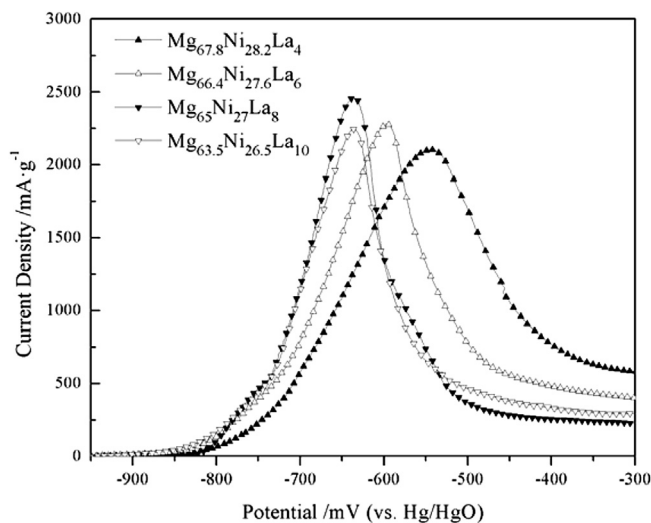
According to above results, the discharge capacity becomes low gradually with the crystallization proceeding of amorphous structure. It indicated that the amorphous structure was a key factor to achieve high discharge capacity and good cycling stability. According to the result of Orimo et al. [23] reported, hydrogen concentrations in three nanometer-scale regions and the maximum hydrogen concentrations of the three regions have been experimentally determined to be 0.3 wt.% H in the grain region of Mg_2Ni, 4.0 wt.% H in the grain boundary and 2.2 wt.% H in the amorphous region. It revealed that the hydrides mainly exist in grain-boundary region and the amorphous phase region. Another explanation for this could be the homogeneous microstructure of the melt spun alloy. The as-cast eutectic alloy charged/discharged for some cycles consisted of lamellae of primary and secondary phases (see Figs. 2 and 11), where long continuous boundaries between primary and secondary phases could act as diffusion paths prior to hydrogen diffusion into the bulk. Zhu et al. [24] also reported that an auto-catalytic effect is might govern the hydriding mechanism of the nanophase composite, while the hydriding process of single
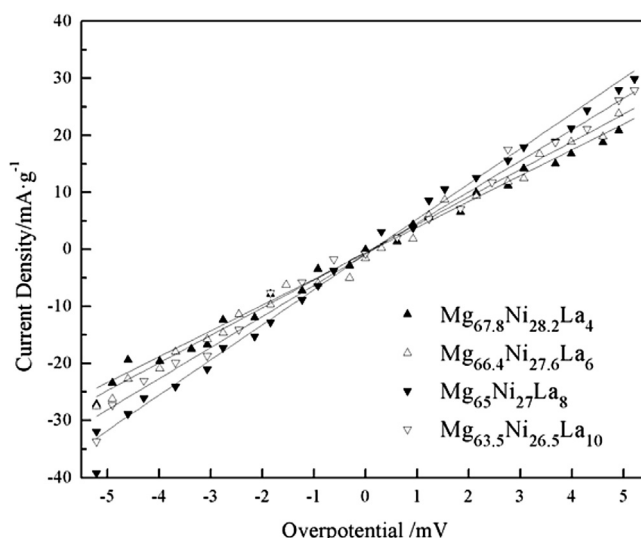

Fig. 5. DSC curves (at 20 °C min⁻¹ heating rate) of amorphous Mg−Ni−La alloys.

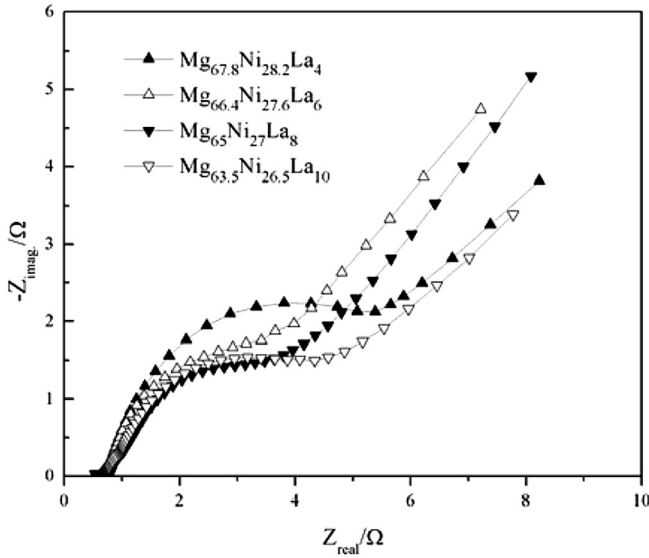Fig. 7. The linear polarization curves of the Mg−Ni−La electrodes.

Fig. 8. Electrochemical impedance spectra of the Mg–Ni–La electrodes at 50% depth of discharge at 27 °C.

component alloys proceeds by means of a nucleation and growth mechanism.

The relationship of discharge potentials (voltage) and the discharge capacities (at the 10 cycles) is shown in Fig. 4. It is seen there that a discharge potentials flat from 0.75 to 0.65 V for each alloy with variation of the discharge capacity which denotes a range of discharge capacity that the alloy can be used. It is found that the discharge capacities of the discharge potential flat have reached more than 400 mAh g^{-1} for alloys Mg$_{65}$Ni$_{27}$La$_8$ and Mg$_{63.5}$Ni$_{26.5}$La$_{10}$. It is also important to point out that the discharge capacity is significantly dependent on the composition and microstructure of the electrode materials.

From the above mentioned, the H-capacity of the Mg–Ni–La alloys in the present study becomes high with the increase of their amorphous phase. Therefore, there must be some relationship between the glass-forming ability (GFA) and the hydrogen capacity of the amorphous Mg–Ni–La alloys. Inoue [25] found that the GFA of the amorphous alloys can be denoted with their super-cooled liquid region ΔT_x ($\Delta T_x = T_x - T_g$, T_x is the crystallization-onset temperature and T_g is the glass-transition temperature). Fig. 5 shows the DSC traces obtained from the Mg–Ni–La amorphous ribbons during heating with a heating rate of 20 °C min^{-1}. The curves of the samples with clear endothermic event are associated with the glass transition followed by a broad, super-cooled liquid region. The T_g and T_x are marked by arrows in the DSC traces. The ΔT_x is also showed in Fig. 5. From Fig. 5, it reveals that both Mg$_{65}$Ni$_{27}$La$_8$ and Mg$_{63.5}$Ni$_{26.5}$La$_{10}$ samples have a broad super-cooled liquid region ΔT_x. It is also seen that the crystallization-onset temperature T_x, the glass-transition temperature T_g and super-cooled liquid region all increase with the La content. It suggests that the stability of amorphous structure of alloys enhances with the increase of La content. It is beneficial to improve the stability of Mg-based alloys.

Fig. 9. Equivalent circuit of the electrodes.

Fig. 6 shows anode polarization curves of the Mg–Ni–La electrodes. In all cases, the anodic current densities increase to a limiting value and then decrease. The anodic peaks correspond to the oxidation of hydrogen, because they are measured at 50% DOD. The limiting current density I_L (an electrochemical kinetics parameter, meaning the speed of mass transfer process in the electrode reaction) is listed in Table 2. It increases first from 2104.4 mA g^{-1} (Mg$_{67.8}$Ni$_{28.2}$La$_4$) to 2458.7 mA g^{-1} (Mg$_{65}$Ni$_{27}$La$_8$) and then decreases to 2246.0 mA g^{-1} (Mg$_{63.5}$Ni$_{26.5}$La$_{10}$), which implies the electrochemical kinetics of the electrodes increases first and then decreases with increasing La content. This illustrates that the diffusion steps play a relatively small role on electrode reaction process for Mg$_{65}$Ni$_{27}$La$_8$ amorphous alloy which shows a relatively fast mass transfer process to better meet the needs of the electrochemical reaction. Among them, Mg$_{65}$Ni$_{27}$La$_8$ electrode has the highest limit current density of 2458.7 mA g^{-1}, that increased by 13% than the value of AB$_3$ type electrode reported [20], which suggests it has good discharge property and reaction kinetics performance.

The exchange current densities I_0 for the electrodes are calculated using the following expression [26]

$$I_0 = I_d \frac{RT}{F\mu} \tag{1}$$

where R, T, I_d, F, μ are the gas constant, the absolute temperature, the applied current density, the Faraday's constant and the total over-potential, respectively. I_d/μ is the slope of these straight lines. Fig. 7 presents the linear polarization curves of the Mg–Ni–La electrodes. One of the biggest slope was Mg$_{65}$Ni$_{27}$La$_8$ electrode, followed by Mg$_{63.5}$ Ni$_{26.5}$ La$_{10}$ electrodes, the smallest is Mg$_{67.8}$Ni$_{28.2}$La$_4$ electrode. Corresponding exchange current density I_0 are listed in Table 2. Mg$_{65}$Ni$_{27}$La$_8$ electrode has the highest exchange current density, reaches 159.6 mA g^{-1}, that implies its good polarization resistance and also explains why Mg$_{65}$Ni$_{27}$La$_8$ electrode discharge voltage is lower than other electrodes.

Fig. 8 shows electrochemical impedance spectra of the Mg–Ni–La electrodes. Each spectrum consists of two semicircles in the high-frequency region followed by a straight line in the low-frequency region. According to literature [27], the small arc in the high-frequency region and the large arc in the low-frequency region were assigned to the contact resistance (R_{cp}) between the current collector (Ni foam) and the alloy particles, and to the charge-transfer reaction resistance (R_{ct}) on the alloy surface, respectively. Using the equivalent circuit presented in literature [28], as shown in Fig. 9, we can calculate the values of four electrodes. The R_s, Z_w and $Q_{1(2)}$ in Fig. 8 represent the solution resistance, the Warburg impedance, and the imperfect capacitor, respectively. The results are listed in Table 3. Both of the R_{cp} and R_{ct} decrease first and then increase with increasing La content. The Mg$_{65}$Ni$_{27}$La$_8$ electrode shows the lowest contact resistance and charge-transfer reaction resistance, suggesting the best electrochemical kinetics.

Fig. 10 shows the DSC curve and the corrected TG curve of the charged Mg$_{65}$Ni$_{27}$La$_8$ alloy powder with heating rate of 5 °C min^{-1}. The DSC curve of the charged sample is quite different from that of uncharged one (Fig. 5). After charging, the crystallization peak disappears and only a continuous but low exothermic band can be observed below 265 °C, accompanied by a continuous desorption of 1.45 wt.% H (because the alloy powder was mixed with nickel powder in a weight ratio of 1:4, see Experimental). It indicates that the amorphous structure of Mg$_{65}$Ni$_{27}$La$_8$ may partially crystallize during hydrogenation. The continuous exothermic band may result from the superposition of the crystallization of residual amorphous phase (exothermic), dehydrogenation of Mg$_{65}$Ni$_{27}$La$_8$ alloy
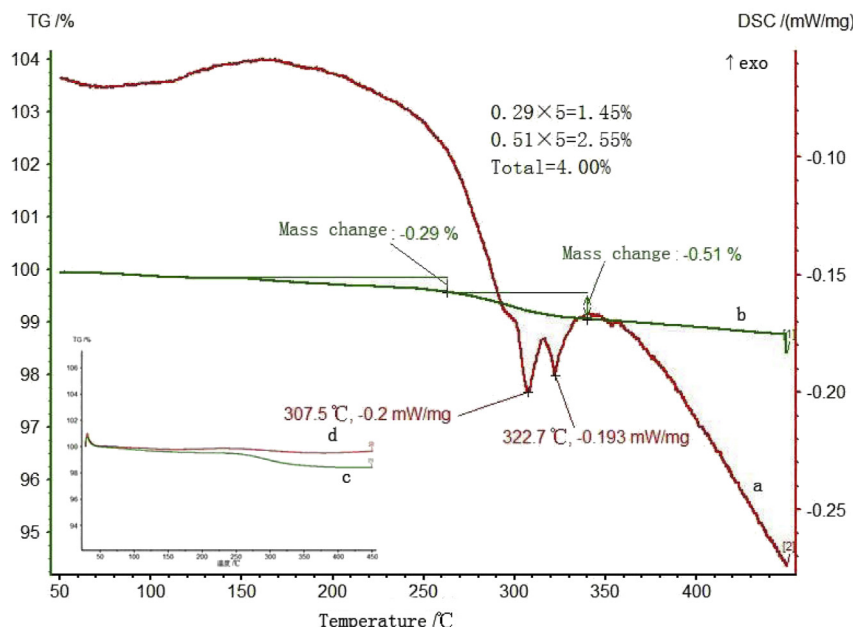
Fig. 10. DSC (a) and corrected TG curves (b) of the charged $Mg_{65}Ni_{27}La_8$ powder at a heating rate of 5 °C min^{-1}. Curve (b) is obtained via multiplying the difference between the TG curves of the charged (c) and uncharged (d) samples by five.

(endothermic), and evaporation of residual water (endothermic). Above 265 °C, two overlapped endothermic peaks are present with peak temperatures of 307.5 and 322.7 °C and end temperature of 341.7 °C. The corresponding mass change is 2.55 wt.%, which implies that another dehydrogenation process occurs. Therefore, the total amount of hydrogen released from the $Mg_{65}Ni_{27}La_8$ alloy is 4.0 wt.%. Combining Fig. 10(a) and (b), the dehydrogenation process of the $Mg_{65}Ni_{27}La_8$ alloy can be divided in two steps, i.e. the first step at low temperature with a desorption of 1.45 wt.% H and the second step at high temperature with a desorption of 2.55 wt.% H.

Fig. 11 shows the XRD patterns of the charged $Mg_{65}Ni_{27}La_8$ sample. Because the sample contains 50 wt.% of nickel powder, three strong characteristic diffraction peaks of Ni are present. It is obvious that Mg_2NiH_4 phase forms during the charging process. The amorphous background concealed by the strong Ni peaks

shows some amorphous phase remains. The crystallinity of $Mg_{65}Ni_{27}La_8$ alloy calculated from Fig. 11 is about 74%, that is, the percentage of residual amorphous phase is 26%. The H atoms in the alloy are mainly stored in two regions, i.e. one part in the amorphous phase and the other part in the Mg_2NiH_4 phase. The crystallization behavior of the $Mg_{65}Ni_{27}La_8$ alloy after hydrogenation is different from the result reported by Spassov and Koster [29], which showed that the hydrogenation slightly decreased the thermal stability but strongly influenced the secondary crystallization of the as-quenched amorphous $Mg_{87}Ni_{12}Y_1$ alloy.

Fig. 12 shows the structural evolution of $Mg_{65}Ni_{27}La_8$ alloy during dehydrogenation at different temperatures. The peaks of Mg_2NiH_4 increases the intensity from Fig. 12(a)–(c), indicating that the amount of Mg_2NiH_4 increases with the rising temperature in the range of 30–250 °C. In combination with Fig. 10(a) and (b) below 265 °C, it is confirmed that the first step of dehydrogenation at low temperature is the hydrogen desorption from the amorphous phase. During this process, a part of hydrogen contained in
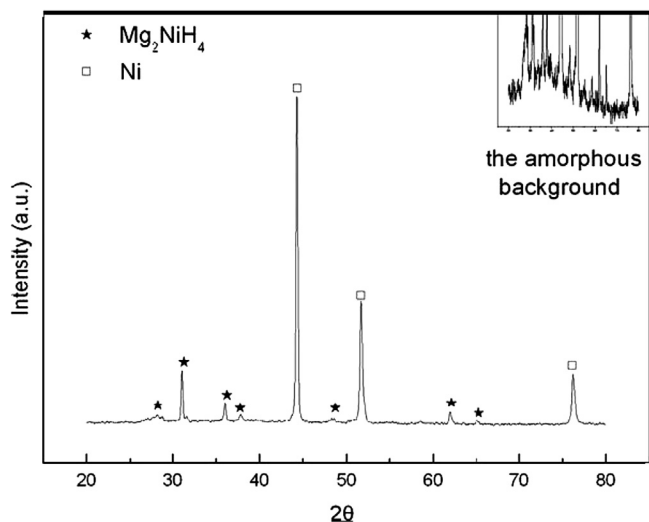

Fig. 11. XRD patterns of $Mg_{65}Ni_{27}La_8$ alloy charged at a current density of 30 mAh g^{-1} for 40 h.

Table 2
Limiting current density I_L (27 °C) and the exchange current densities I_0 for the Mg–Ni–La alloy electrodes.

Samples	I_L/mA g^{-1}	I_0/mA g^{-1}
$Mg_{67.8}Ni_{28.2}La_4$	2104.4	117.3
$Mg_{66.4}Ni_{27.6}La_6$	2278.8	125.4
$Mg_{65}Ni_{27}La_8$	2458.7	159.6
$Mg_{63.5}Ni_{26.5}La_{10}$	2246.0	141.1

Table 3
Contact resistance R_{cp} and charge-transfer resistance R_{ct} of the Mg–Ni–La alloy electrodes at 27 °C.

Samples	R_{cp}/Ω	R_{ct}/Ω
$Mg_{67.8}Ni_{28.2}La_4$	1.02	5.38
$Mg_{66.4}Ni_{27.6}La_6$	0.98	3.96
$Mg_{65}Ni_{27}La_8$	0.99	3.36
$Mg_{63.5}Ni_{26.5}La_{10}$	1.10	3.79

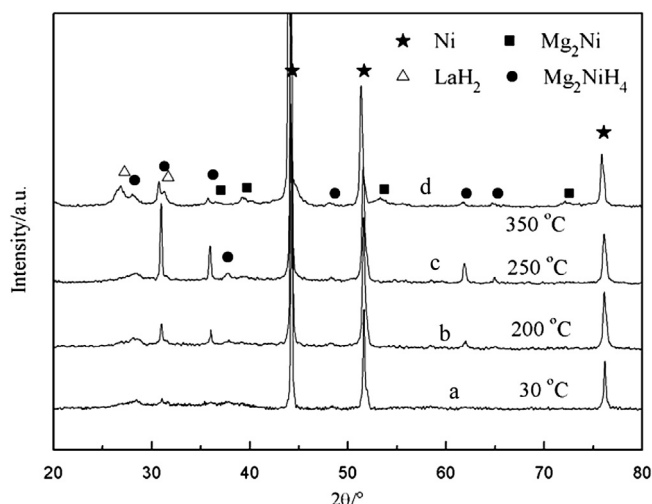**Fig. 12.** XRD patterns of the charged $Mg_{65}Ni_{27}La_8$ sample annealed at 30 °C (a), 200 °C (b), 250 °C (c) and 350 °C (d).

the amorphous phase is released to the atmosphere while another part reacts with Ni and Mg nucleating the Mg_2NiH_4 phase. Therefore, after charging the amount of H atoms dissolved in the amorphous phase is over 1.45 wt.%, which is 36% of the total amount of hydrogen absorbed by the sample. Taking into account that the amount of amorphous phase is only 26%, a conclusion could be drawn that the hydrogen storage capacity of amorphous phase is larger than that of Mg_2NiH_4. The intensity of the Mg_2NiH_4 peaks in Fig. 12(d) obviously decreases compared with those of Fig. 12(c) and the peaks of LaH_2 and Mg_2Ni are present, indicating the dehydrogenation of Mg_2NiH_4 into Mg_2Ni and the formation of LaH_2. It is revealed that the second step of dehydrogenation with a mass loss of 2.55 wt.% is caused by the decomposition of Mg_2NiH_4 into Mg_2Ni, and the formation of Mg_2Ni and LaH_2 are responsible for the two endothermic peaks at 307.5 and 322.6 °C (Fig. 9(a)).

4. Conclusions

The effects of microstructure on the electrode properties of the rapidly solidified Mg−Ni−La amorphous alloy were examined and the detailed investigation on the microstructure evolution in the dehydrogenation process of the $Mg_{65}Ni_{27}La_8$ alloy. The results obtained are summarized as follows:

(1) The effects of different contents of La are discussed on the basis of discharge-capacity, the morphology, limiting current density and electrochemical impedance spectra of the Mg−Ni−La electrodes. The $Mg_{65}Ni_{27}La_8$ alloy exhibits the best reaction kinetics performance, the lowest contact resistance, a maximum discharge capacity of 582 mAh g^{-1} at room temperature and releases 4.0 wt.% H during the non-isothermal dehydrogenation process.

(2) The non-isothermal dehydrogenation process of the alloy can be divided in two steps, corresponding to the dehydrogenation of amorphous phase and Mg_2NiH_4, respectively.

(3) During charging, the amorphous phase is transformed in Mg_2NiH_4. The amount of H solute atoms dissolved in the amorphous phase is over 1.45 wt.%, which is 36% of the total amount of hydrogen absorbed by the sample. The hydrogen storage capacity of the amorphous phase is larger than that of Mg_2NiH_4.

References

[1] L. Schlapbach, A. Züttel, Nature 414 (2001) 353−358.
[2] A. Züttel, Mater. Today 9 (2003) 24−33.
[3] I.P. Jain, Int. J. Hydrogen Energy 34 (2009) 7368−7378.
[4] B. Sakintuna, F. Lamari-Darkrim, M. Hirscher, Int. J. Hydrogen Energy 32 (2007) 1121−1140.
[5] F.Y. Cheng, Z.L. Tao, J. Liang, J. Chen, Chem. Commun. 48 (2012) 7334−7343.
[6] N.S. Norberg, T.S. Arthur, S.J. Fredrick, A.L. Prieto, J. Am. Chem. Soc. 133 (2011) 10679−10681.
[7] R.W.P. Wagemans, J.H.V. Lenth, P.E. Jongh, A.J.V. Dillen, K.P. Jong, J. Am. Chem. Soc. 127 (2005) 16675−16680.
[8] A. Zaluska, L. Zaluski, J.O. Strom-Olsen, J. Alloys Compd. 288 (1999) 217−225.
[9] G. Barkhordarian, T. Klassen, R. Bormann, J. Alloys Compd. 364 (2004) 242−246.
[10] Z. Dehouche, T. Klassen, W. Oelerich, J. Goyette, T.K. Bose, R. Schulz, J. Alloys Compd. 347 (2002) 319−323.
[11] M.Y. Song, I.H. Kwon, S.N. Kwon, C.G. Park, H.R. Park, J.S. Bae, Int. J. Hydrogen Energy 31 (2006) 43−47.
[12] J.W. Liu, L.F. Jiao, H.T. Yuan, Y.J. Wang, Q. Liu, J. Alloys Compd. 403 (2005) 270−276.
[13] B. Khorkounov, A. Gebert, C. Mickel, L. Schultz, J. Alloys Compd. 416 (2006) 110−117.
[14] X.Z. Xiao, X.H. Wang, L.H. Gao, W. Li, C.P. Chen, J. Alloys Compd. 413 (2006) 312−318.
[15] L.J. Huang, G.Y. Liang, Z.B. Sun, J. Power Sources 160 (2006) 684−687.
[16] L.J. Huang, G.Y. Liang, Z.B. Sun, Y.F. Zhou, J. Alloys Compd. 432 (2007) 172−176.
[17] L.J. Huang, Jian-guo Tang, G.Y. Liang, Yao Wang, D.C. Wu, J. Power Sources 189 (2009) 1247−1250.
[18] L.J. Huang, Jian-guo Tang, Yao Wang, Ji-xian Liu, D.C. Wu, J. Alloys Compd. 485 (2009) 186−191.
[19] H.G. Pan, Y.F. Liu, M.X. Gao, Intermetallics 13 (2005) 770−778.
[20] F.L. Zhang, Y.C. Luo, J.P. Chen, J. Power Sources 150 (2005) 247−254.
[21] F.X. Wang, X.P. Gao, Z.W. Lu, J. Alloys Compd. 370 (2004) 326−330.
[22] C. Rongeat, L. Roué, J. Power Sources 132 (2004) 302−308.
[23] S. Orimo, H. Fujii, Appl. Phys. A 72 (2001) 167−173.
[24] M. Zhu, Y. Gao, Z.X. Che, Y.Q. Yang, C.Y. Chuang, J. Alloys Compd. 330 (2002) 708−715.
[25] A. Inoue, Acta Mater. 48 (2000) 278−306.
[26] P.H.L. Notten, P. Hokkeling, J. Electrochem. Soc. 138 (1991) 1877−1885.
[27] N. Kuriyama, T. Sakai, H. Miyamura, I. Uehara, H. Ishikawa, T. Iwasaki, J. Alloys Compd. 202 (1993) 183−197.
[28] Q. Liu, L.F. Jiao, H.T. Yuan, Y.J. Wang, Y. Feng, J. Alloys Compd. 427 (2007) 275−280.
[29] T. Spassov, U. Koster, J. Alloys Compd. 287 (1999) 243−250.